

Phase-modulation laser interference microscopy: an advance in cell imaging and dynamics study

Alexey R. Brazhe

Nadezda A. Brazhe

Technical University of Denmark
Department of Physics
2800 Kongens Lyngby, Denmark
and

Moscow State University
Biophysics Department
Biology Faculty
Leninskie Gory 1, Building 12
119991 Moscow, Russia

Georgy V. Maksimov

Moscow State University
Biophysics Department
Biology Faculty
Leninskie Gory 1, Building 12
119991, Moscow, Russia

Pavel S. Ignatyev

Amphora Laboratory
5th Bolshaya Magistralnaya str.
123007, Moscow, Russia

Andrey B. Rubin

Moscow State University
Biophysics Department
Biology Faculty
Leninskie Gory 1, Building 12
119991, Moscow, Russia

Erik Mosekilde

Olga V. Sosnovtseva

Technical University of Denmark
Department of Physics
2800 Kongens Lyngby, Denmark

1 Introduction

Noninvasive studies of living cells are important for basic biological research as well as for applications in medicine and drug development. Traditional techniques such as electrophysiology or fluorescent microscopy are more or less damaging due to the penetration of the microelectrode through the cell membrane or due to the use of contrasting or fluorescent dyes. For these reasons novel techniques based on the measurement of cellular intrinsic optic properties (IOPs) have become increasingly popular during the last decades.

Cohen et al. observed changes in the light scattering intensity from a nerve during its electrical activity,¹ and Stepnoski et al. showed that the intensity of light scattered by the mollusc *Aplisia* neurons depends linearly on the transmembrane

Abstract. We describe how phase-modulation laser interference microscopy and wavelet analysis can be applied to noninvasive non-stained visualization and study of the structural and dynamical properties of living cells. We show how phase images of erythrocytes can reveal the difference between various erythrocyte forms and stages of hemolysis and how phase images of neurons reveal their complex intracellular structure. Temporal variations of the refractive index are analyzed to detect cellular rhythmic activity on different time scales as well as to uncover interactions between the cellular processes. © 2008 Society of Photo-Optical Instrumentation Engineers. [DOI: 10.1117/1.2937213]

Keywords: biomedical optics; microscopy; imaging; interferometry; wavelet transforms; coherent optical systems.

Paper 07284RR received Jul. 27, 2007; revised manuscript received Jan. 22, 2008; accepted for publication Jan. 22, 2008; published online Jun. 26, 2008.

potential.² By now it is clear that the optic properties of cells depend not only on the electric activity and ion fluxes but also on the cell volume and shape and on the cellular compartmentalization.³ The light scattering detection became rather popular for noninvasive study of neuronal electrical activity. For instance, coherence tomography, based on the registration of the light scattering intensity, has been applied for visualization of neural tissue morphology and for detection of optical changes during electrical excitation.⁴ However, light scattering signals are relatively weak compared to practical detection limits and therefore difficult to observe without extensive signal averaging. Alternative methods for IOP measurements are various types of interferometric techniques that make it possible to obtain quantitative information on the refractive index (RI). The RI is one of the cell characteristics, underlying IOPs, and containing valuable information about

Address all correspondence to A. Brazhe, Physics Technical University of Denmark, 309, DTU Campus-Lyngby, 2800 Denmark; Tel: +45 45253248; Fax: +45 45931669; E-mail: brazhe@fysik.dtu.dk, brazhe@biophys.msu.ru

cellular compartmentalization and processes. As various cell structures have different RI values, they retard propagating light differently. Measurement of the resulting phase shifts with consequent reconstruction of the cell phase images with submicron resolution is realized with different types of interference microscopy: laser interference microscopy,⁵ digital holographic microscopy,⁶ Fourier phase microscopy, Hilbert phase microscopy, diffraction phase microscopy and others.⁷⁻¹⁰

The phase image of an object depends on its thickness and refractive index. The latter is dependent on the properties of the plasma membrane and organelles and cytoplasm compartmentalization. Dynamical study of phase images is therefore a very promising noninvasive approach to cell research. Most recent studies in this area focus either on the investigation of relatively slow changes in the cell thickness⁹ (up to 0.5 Hz) or on fast measurements (with millisecond resolution) of the optical path length without further frequency analysis.⁸ Some of the studies focus on the dynamical morphometry.⁶ It is now evident that interference and quantitative phase microscopes provide valuable information about cell thickness and volume, as well as about intracellular structures. However, most approaches to the phase image analysis leave quite a lot of valuable information about cell compartmentalization and dynamics behind. Obviously, there is a need in a deeper insight in “biological mechanisms” underlying changes in IOPs. The comparison of the observed phase images with the dynamical state of a cell and its structures is a necessity.

We consider it an important part of an interferometric study to combine phase imaging with advanced data analysis techniques to proceed in understanding of the cellular rhythmic processes and reveal their characteristic periods and mutual interactions. We have previously shown the existence of pronounced frequencies in variations of the local refractive index of excitable and nonexcitable cells (neurons, mast cells and erythrocytes) by means of laser interference microscopy and wavelet analysis.^{11,12} The purpose of this paper is to report our data on the application of the phase-modulation laser interference microscopy (PM-LIM) to the imaging of neurons and different types of erythrocytes on various hemolysis stages, and to provide a more detailed analysis of the local phase dynamics.

2 Theory of the Phase-Modulation Laser Interference Microscopy

The results discussed here were obtained with the phase-modulation laser interference microscope MIM 2.1. The microscope was developed by the Amphora Laboratories company^{5,13} (Moscow, Russia). Its application to biomedical purposes was advanced in a close collaboration with the Biophysics Department at Moscow State University.

The MIM 2.1 setup is a combination of two optical schemes: one channel is a classical white light microscope, which works in the reflected light, and the other channel is a laser microinterferometer. The setup can be switched between the two modes of operation. The white light mode is used for navigation and adjustment of the sample, and the interferometric mode is used for high-resolution imaging and time-resolved measurements. The laser channel unit is a modified Mach-Zehnder microinterferometer with reference wavefront

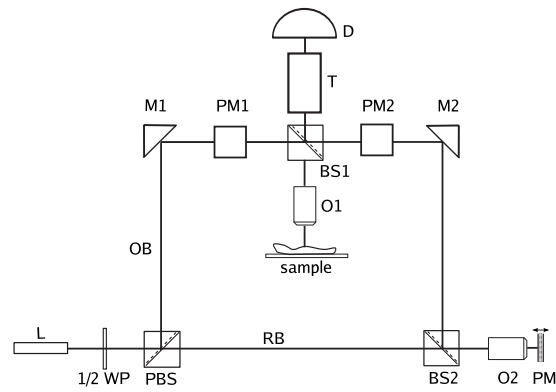


Fig. 1 Scheme of MIM 2.1 phase-modulation laser interference microscope: L, light source; 1/2 WP, half wave plate; PBS, polarizing beam splitter; RB and OB, reference and object beams; respectively; D, detector; PM, reference phase-modulation mirror; T, telescopic system; BS, beamsplitters; M, mirrors; O, objectives; and PM polarizing modulators.

modulation. A 532-nm solid state laser with 40 W output power is used.

The basic principles of MIM 2.1 are the following (see Fig. 1). The collimated beam from the laser (L) comes through the motorized half-wave plate to be divided into the object beam (OB) and the reference beam (RB) on the polarizing beamsplitter (PBS). The ratio of light intensity distribution between OB and RB can be operated with the rotation of the half-wave plate.

Object beam goes through the objective O1, nonpolarizing beamsplitter BS1 and the telescopic system T. Reference beam is reflected from the phase-modulation mirror PM and forms the reference wavefront via the objective O2, nonpolarizing beamsplitter BS2 and the telescopic system. The piezo-driven phase-modulation mirror (PM) is located near the focal plane of the objective O2. Object and reference wavefronts form the interference image on the CMOS photosensor plate D. The pixelwise analysis of the interferogram is operated by a PC computer. The operating software was developed at Amphora laboratories.

The light intensity of the interference signal is defined by the well-known formula:

$$I = A_0^2 + A_{\text{obj}}^2 + 2A_0A_{\text{obj}} \cos(\phi_0 - \phi_{\text{obj}}), \quad (1)$$

where A_0 and ϕ_0 and A_{obj} and ϕ_{obj} are the amplitude and the phase of the reference and object beam, respectively. Most interferometer imaging systems reconstruct phase height profile of an object from the whole acquired image or series of images. This can lead to certain ambiguities in reconstruction for such complex objects as live cells normally are, or the measurement can be hindered in the regions where the intensity is low, near the level of noise. To avoid these problems in MIM 2.1 microscope, the phase shift is determined independently for each pixel of the photosensitive camera. The length of the reference beam arm is harmonically modulated at 500 Hz. The measurements are done measured pixel after pixel in an independent manner. For each pixel the intensity I is measured as a function of the position of the phase-modulation mirror (PM). The intensity varies with the PM

movement and we find the PM position which corresponds to the point of the maximal rate the I change. The use of a calibrated piezomodulator makes it possible to determine the precise position of the PM, this is discussed in more details in Ref. 13. The phase of the reference beam in this position of the modulation mirror is offset by $\pi/2$ relative to the phase of the object beam. Thus, optical path differences (OPD) are obtained independently for each pixel. They can be described by

$$\Phi_{\text{obj}} = \frac{\phi_0 - \phi_i \lambda}{2\pi} - \Phi_0. \quad (2)$$

Here ϕ_0 and λ are the initial phase and the wavelength of the laser beam, respectively; ϕ_{obj} stands for the phase in the presence of the object; Φ_0 is a constant phase shift determined by the choice of the phase reference point; and Φ_i values at all points of an object constitute the OPD relief or, in other words, the phase image of the object. To eliminate external artificial disturbances, the channel for the subtraction of the artificial low-frequency vibrations was used. This active vibroisolation is realized as an additional photodiode, placed near the CCD array, it receives light from the region adjacent to the working viewfield and the signal from it is subtracted from the signal, obtained from the CCD. Thus, any vibrations, inducing movements of the specimen as a whole, are neglected.

The detector D is a 1024×1024 -pixel CMOS photosensitive matrix, and Φ values are measured independently in each pixel with the rate 500 pixels/s. It is possible to work with other sizes and shapes of the frame, from 1×1 to 1024×1024 . In this paper, we used an objective with a numerical aperture (NA) of 0.15 ($\times 27$). The interference working field was $27 \times 27 \mu\text{m}$, equal to 256×256 pixels, so the capture time of a single image was 131 s ($256 \times 256 / 500$). As already mentioned, the phase shift is measured independently in each pixel due to the modulation of position of the reference phase-modulation mirror, so the phase image is constructed as a result of measurements of the Φ value in each point.

The lateral resolution of MIM 2.1 mainly depends on the objective NA, but also on the phase contrast of the studied sample (the difference between RI values in the neighboring points) and the level of noise, mostly of the detector. For the objective used, the lateral resolution was $2.16 \mu\text{m}$. Note that the same MIM 2.1 setup can provide lateral resolution better than 100 nm for objectives with a high NA. We refer here to the superresolution in interference microscopy, which is related to phase dislocations inside the diffraction-limited spot.^{5,14,15} Phase dislocations (phase singularities) can be seen in the regions of high phase gradients in an object. Theoretical explanation of this “superresolution” was given by Totzeck and Tiziani.^{16,17} The resolution in interference microscopy is thus objective and object dependent.

In this paper, we used low NA objective, as it provides better depth of focus (T), than high-NA objectives:

$$T = \frac{n\lambda}{(\text{NA})^2}, \quad (3)$$

where n is the refractive index of the immersion ($n=1$ for the dry objective). The detailed characteristics and description of

the MIM 2.1 setup, reconstruction procedure, and examples of the microrelief measurement can be found in Refs. 13 and 18. Note that in our previous works^{11,12} MIM 2.1 was based on the Linnik interferometer, however, the principles of operation and phase image reconstruction were the same as in the setup presented in this paper.

3 Experimental Details

To verify that there is no photodamage induced by the laser illumination we tested the cells for the absorbance in the region of 532 nm. No light absorption was found in this region, thus, photodamage is not likely to take place. Both neurons and erythrocytes were stable under illumination during 2 to 3 h, which is significantly longer than the duration of the experiment. The laser power per cell (with diameter about $50 \mu\text{m}$) was less than 1 mW.

All studied cell types have good adhesive properties to the mirror surface and therefore stuck to the bottom chamber layer. Cell position was tracked respectively to ticks on the mirror, so that any small movements of the cell along the mirror could be noted. None of the neurons and/or erythrocytes possess fringelike movements at the edge, so such small, hardly detectable movements can be not taken into account. The shape and area of the cell were monitored in the white light mode of the setup and during experiments we did not observe any changes of the parameters described.

We used the following preparations: human blood from healthy donors (taken in accordance with the standards of the Ethics Committee of Russian Institute of Clinical Cardiology), blood from the grass frog *Rana temporaria*, and neurons isolated from the ganglia of the snail *Lymnaea stagnalis* and medical leech *Hirudo medicinalis*. A drop of blood or isolated neurons were placed into the containment chamber with mirror bottom layer filled with buffer for erythrocytes (mM: 145 NaCl, 5 KCl, 1 CaCl₂, 1 MgSO₄, 4 Na₂HPO₄, 1 NaH₂PO₄, 10 glucose, pH 7.4), physiological solution for the snail neurons (mM: 50 NaCl, 1.5 KCl, 4 CaCl₂, 1 MgCl₂, 11 HEPES, pH 7.5) or leech neurons (mM: 150 NaCl, 4 KCl, 1.8 CaCl₂, 1 MgCl₂, 11 HEPES, pH 7.4).

4 Cell Visualization

Let us first demonstrate how PM-LIM can be used to investigate the functional state of a cell. As examples we chose cells with a soft surface and complicated compartmentalization (neurons) and cells with a rigid cytoskeleton, tough membrane, and simple intracellular structure (erythrocytes).

Figures 2(a) and 2(b) present the phase images of two erythrocyte types: a discocyte and an early-stage echinocyte, respectively. A discocyte is a normal form of erythrocyte that most erythrocytes have. During the early hemolysis stage or influence of certain chemicals (e.g., surface-active drugs) discocytes change their form to echinocytes. Phase profiles of discocyte and echinocyte in the marked regions are shown in Figs. 2(c) and 2(d). The difference between these two erythrocytes is clear: the discocyte has a typical toroidal form and the echinocyte has a rough discoid structure with protuberances. Besides, the echinocyte, compared to the discocyte, has a significantly higher OPD, which results from the difference in the cells shape and cytoskeleton structure, the protrusions in the echinocyte and also from the different distributions of

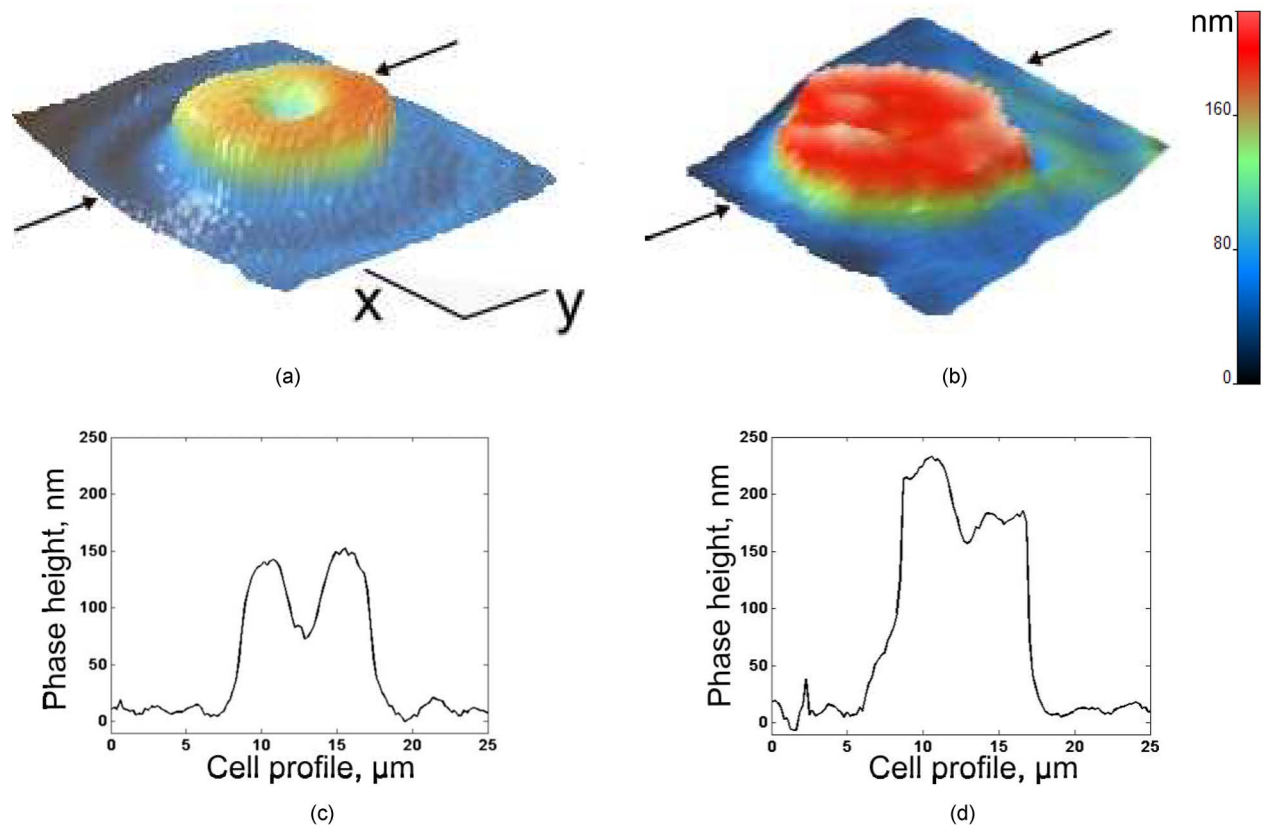


Fig. 2 Phase images of human erythrocytes: (a) discocyte and (b) echinocyte. The color bar indicates optical path difference in nm (color online only). The x and y bars both measure $5\ \mu\text{m}$. (c) and (d) OPD profiles of the discocyte and the echinocyte, respectively, along the line marked by arrows.

hemoglobin (Hb) inside the cells. It is known that various forms of erythrocytes can be distinguished by means of conventional microscopy. Our results serve to demonstrate, that PM-LIM phase images provide information that is at least similar to that from conventional microscopy. Besides, interference microscopy can be used as an additional technique to monitor erythrocyte forms because of its sensitivity to changes in the cells shape and intrinsic optical properties. For example, we have shown previously that phase images can reveal differences between discocytes that are indistinguishable in photographs, obtained in reflected white light.¹²

Human erythrocytes (as well as those of other mammals) lack nuclei and major organelles. This makes their phase images relatively simple to interpret. Nucleated erythrocytes have a much more complex structure and, therefore, represent an interesting preparation for the interference imaging. It is known that the nucleus of a frog erythrocyte can contain hemoglobin in a concentration that depends on the stage of hemolysis.¹⁹ Figure 3 shows phase images of nucleated frog erythrocytes at different stages of hemolysis. The nucleus in the intact erythrocyte does not contain Hb, hence the OPD of the nuclear region is lower than that of the cytoplasm and the image looks like a doughnut [Fig. 3(a)]. Under hemolysis the plasma membrane is disrupted and the nucleus membrane is also damaged. As a result, hemoglobin leaks from the cell and can also enter into the nucleus. Thus, different stages of hemolysis can be characterized by different distributions of Hb between nucleus and cytoplasm.¹⁹

This is apparent in the distribution of the OPD. Figure 3(b) presents the phase image of the frog erythrocyte when OPD distribution suggests that the RI in the cytoplasm is less than in the nucleus due to the Hb leakage from the cytoplasm to the outside of the cell and to Hb influx into the nucleus. One can see that the OPD of the nuclear region is significantly higher than that of the surrounding cytoplasm. During the next hemolysis stage, Hb and other proteins (and, therefore, the RI) are more uniformly distributed among nucleus and cytoplasm, so the nucleus “disappears” in the phase image

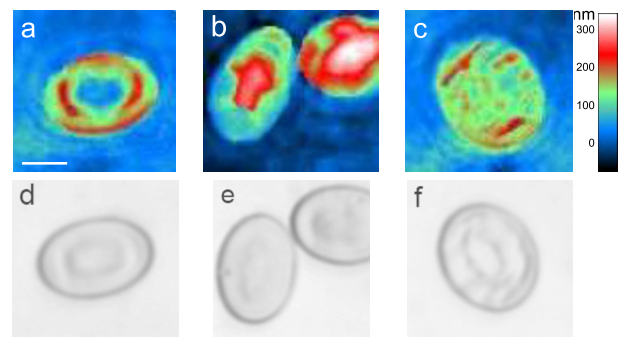


Fig. 3 Phase images of frog erythrocytes (a) in control and (b) and (c) during different hemolysis stages. The color bar indicates the OPD in nm. (d), (e), and (f) Corresponding photographs of erythrocytes in the reflected white light. The horizontal bar is $10\ \mu\text{m}$ (Color online only).

[Fig. 3(c)]. Regions with higher OPD (red areas) may correspond to the islets of residual Hb left after hemolysis and/or to the roughness of the erythrocyte surface that could have arisen due to disruption of the plasma membrane integrity [Fig. 3(c)]. Observed phase images of frog erythrocytes are in a full agreement with the images obtained by phase-contrast microscopy at various hemolysis stages.¹⁹ Note also that differences between hemolysis stages that can hardly be seen in photographs of cells in the reflected light [Figs. 3(d) and 3(e)] are very pronounced in PM-LIM phase images [Figs. 3(a) and 3(b)].

In the example of nucleated frog erythrocytes we show that PM-LIM can be successfully used to visualize the relatively homogeneous cells with distinguished nucleus and to monitor the redistribution of the refractive index inside such cells. However, most cells (for example, neurons, secretory and immune cells, etc.) are highly inhomogeneous and feature a complicated structure of cytoskeleton, Golgi apparatus and vesicles, branching net of endoplasmic reticulum, and mitochondria. Such complicated intracellular structures can produce difficulties if one makes reconstructions from the whole interference image.

Our next example serves to demonstrate how PM-LIM can be used to visualize complicated inhomogeneous cells like neurons. It is evident that neurons represent important objects for a noninvasive IOP study. First, it is a challenge to visualize neuronal structure without contrasting dyes. Second, neurons can be considered as “soft cells” and can hardly be visualized by means of atomic force microscopy. Several studies of neuron imaging by means of digital holographic and interference microscopies have been reported recently.^{6,12,20,21} Rappaz et al., for example, elegantly showed how digital holographic microscopy can be used for the calculation of the RI and thickness of neurons.⁶

The next part of this paper concerns the spatial distribution of the local refractive index and its relation to the cell structures. Figure 4 presents phase images of the axon hillock region of a snail neuron [Fig. 4(a)] and a nonmyelinated axon [Fig. 4(b)] and corresponding photographs in the reflected light. Snail neurons have a smooth shape after isolation, and the OPD relief reveals the landscape of various organelles, the cytoskeleton and the plasma membrane structures. The highest (white) points in the phase image indicate the highest optical density. The complex inhomogeneous structure of the neuron cytoplasm in the region of the axon hillock can be more clearly seen in the phase image [Fig. 4(a)] than in the ordinary photograph [Fig. 4(c)]. The smoothness of the phase image of the axon indicates its simpler organization, in particular the absence of large organelles and specific compartmentalization.

5 Analysis of the Refractive Index Dynamics

To illustrate application of PM-LIM to the dynamical studies of cell processes this section presents results for the analysis of the optical path difference dynamics in neurons and erythrocytes. As briefly discussed in the theory of Sec. 2, it seems very likely that under the present experimental conditions, the main input to the OPD changes was from the changes in the RI.

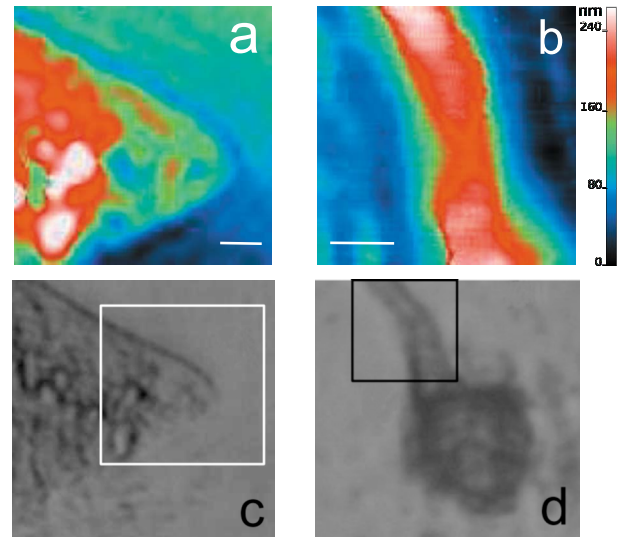


Fig. 4 Phase images of neurons with (a) axon hillock and (b) axon, and (c) and (d) corresponding photographs of the neuron and axon in the reflected light. The color bar indicates OPD in nanometers (color online only). The white horizontal bars are 5 μm .

5.1 Wavelet Analysis of Data

The dynamical reorganization of membrane structures along with cytoplasm compartmentalization and changes in the position and shape of organelles alter the local values of the refractive index and sometimes cellular shape and volume. As discussed, the OPD depends on both the RI and the cell size and is determined by

$$\Phi(x, y) = \int_0^Z [n_{\text{obj}}(x, y, z) - n_s] dz - \Phi_0, \quad (4)$$

where n_s is the (constant) RI of the physiological saline, $n_{\text{obj}}(x, y, z)$ is the RI of the cell at the (x, y) point a distance z from the mirror, and Z is the upper limit of integration that is chosen as a point above the cell.

As suggested by the general form of the phase height differential, $d\Phi = Zdn + (n - n_s)dZ$, when the changes in the cell thickness are relatively small, the OPD dynamics is mainly determined by variations in the RI. For a typical neuron, we have⁶ $n = 1.38$, and the RI of the physiological solution is $n_s = 1.34$ and $Z \approx 10 \mu\text{m}$; if we then consider 1% changes in Z and in n , we obtain $Zdn \approx 0.14 \mu\text{m}$ and $(n - n_s)dZ \approx 0.004 \mu\text{m}$. The cells were at intervals monitored in the white-light operation mode and we hardly observed any changes in the cell shape or geometry. Thus, we can conclude that the measured variations in the OPD were dominated by the dynamics of the RI. Besides, all experiments were performed under normal conditions without modification of the solution osmolarity or application of drugs that are known to modify cell volume or shape, so there were no premises for the pronounced changes of the cell geometry to occur.

The independent pixelwise recording and reconstruction of the OPD used in MIM 2.1 enables us to study the local dynamics of RI at any cellular region with a stable sampling rate. The rate of OPD measurement is 500 pixels/s, so the sampling interval for each point depends on the number of

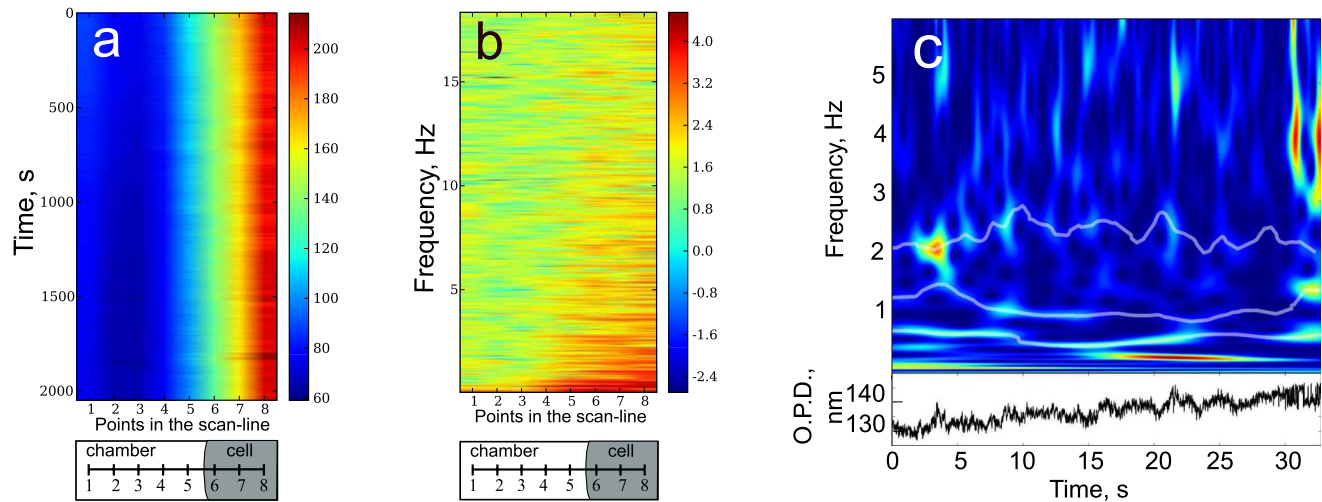


Fig. 5 (a) Upper figure: evolution in time of the optical path difference along the scan line crossing the neuron; X axis, points of the scan line; and Y axis, time in seconds. The color bar represents OPD in nanometers. (a) and (b) Bottom figures are schemes of the scan line crossing the neuron. Length of the scan line in all cases was $6 \mu\text{m}$. (b) Upper figure: power spectral density of OPD variations in the scan line points on the same neuron; X axis, points of the scan line, Y axis, frequency in hertz. Color bar represents logarithm of the frequency power. In-between points along the scan line are linearly interpolated. (c) Upper figure: scalogram for the OPD dynamics in the sixth point of the scan-line corresponding to the membrane region of the neuron. White curves show selected rhythms. Colors indicate the power of frequencies. (c) Bottom figure: time-dependence of the OPD variations on the sixth point of the scan line; X axis (upper and bottom figures); time in seconds; Y axis in the upper figure, frequency in hertz; Y axis in the bottom figure, OPD in nanometers.

points in the studied region or line. In this work, data acquisition was performed in a horizontal scan [Fig. 5(a), bottom figure] of 8 points with a sampling interval for individual point of 16 rms. The scan line was drawn across the neuron boundary so that first five points were distributed in the bottom layer of the chamber and the three last points at the neuron boundary [Fig. 5(a), bottom figure]. The same scheme of the scan line drawing was applied to erythrocytes. Points were uniformly distributed along the scan line by the microscope software. The number of measurements in each point was 2048 and the total time of the OPD measurement in all points of the scan line was 33 s.

Regular cooperative processes inside the cell are assumed to lead to regular changes in the RI. Apparently, any regular vesicle movement chains along the microtubules, or changes in the membrane fluidity and the clustering of membrane-bound channels etc. tend to manifest through the RI. Thus, our working hypothesis was that observable rhythms in the RI dynamics can be ascribed to individual cellular processes and their interactions. Indeed, this is not achievable in a single study and here we give only a few examples.

Investigation of the characteristic frequencies of RI variations in different cell types provides valuable information about various cellular processes. To study multimode dynamics in neurons and erythrocytes we applied wavelet-data analysis.¹¹ The advantages of this approach in comparison with the classical Fourier transform have been widely discussed.²² The wavelet transform of a signal $x(t)$ is determined by

$$T_x(a, t) = \frac{1}{\sqrt{a}} \int_{-\infty}^{\infty} x(u) \psi^* \left(\frac{u-t}{a} \right) du. \quad (5)$$

Here ψ is a “mother” function that should be soliton-like with a zero average, and the asterisk (*) denotes complex conjugation;

$T_x(a, t)$ are the wavelet coefficients; and a is the time scale. The details of the transform (e.g., the choice of ψ) depend on the problem to be solved. In the analysis of rhythmic components, the Morlet function is typically considered. A simplified expression of the Morlet wavelet has the form

$$\psi(\tau) = \pi^{-1/4} \exp(j2\pi f_0 \tau) \exp\left(-\frac{\tau^2}{2}\right), \quad (6)$$

where j is the imaginary unit, and the value f_0 enables us to search for a compromise between the localization of the wavelet in the time and frequency domains. In our work, f_0 equals 1.0 in the low-frequency range (0 to 6 Hz) and 5.0 in high-frequency range (6 to 30 Hz). The relation between the scale a and the central frequency for the mother function f in this situation is $f \approx f_0/a$. The analyzed frequencies interval was 0.08–30 Hz.

For the detailed description of the data-series analysis and experimental procedure see Ref. 12. For the wavelet analysis and data visualization we have developed an open source software iWand (<http://iwand.sf.net>).

5.2 Rhythmic Processes in Neurons and Erythrocytes

Figure 5 (a, upper graphics) presents the evolution in time of the optical path difference along the scan-line crossing the leech neuron. The “cell” and “chamber” points are clearly distinguishable as their OPD values are significantly different. A standard procedure for the fast Fourier transform was applied to investigate frequencies of OPD variations at all points of the scan line. Pronounced frequencies of OPD variations can be observed only in the “cell” points (the sixth to eighth) and partly in the fifth point but not in other “chamber” points [Fig. 5 (b, upper graphics)]. Importantly, that cell can be eas-

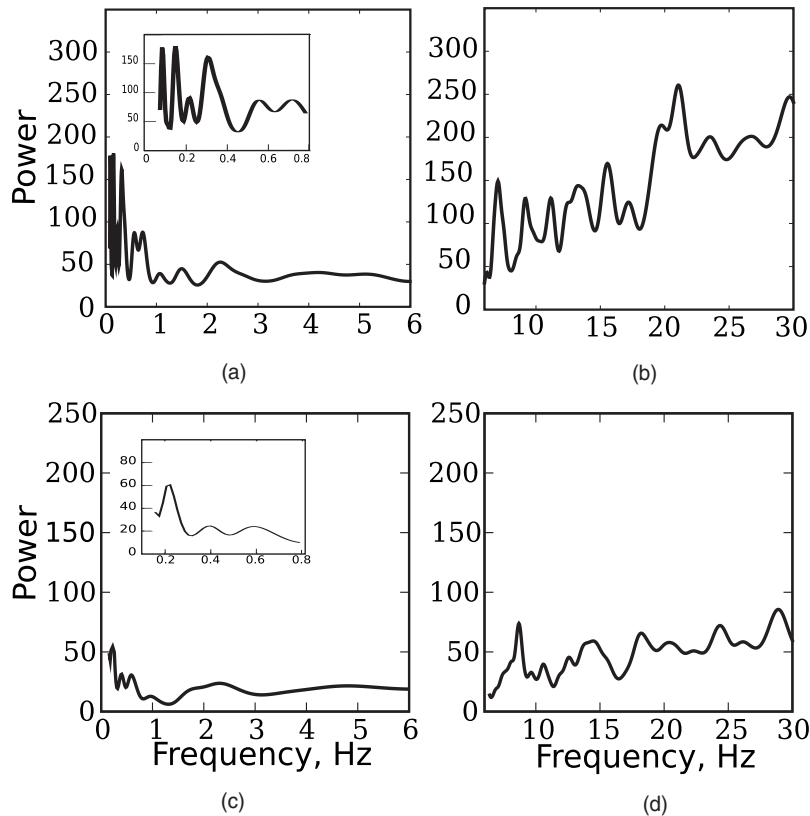


Fig. 6 (a) and (b) Time-averaged power spectra of the refractive index dynamics in the boundary region of the leech neuron (sixth point of the scan line in Fig. 5) and (c) and (d) averaged power spectra of RI dynamics in the boundary region of the human erythrocyte. Inset figures in (a) and (c) show enlarged parts of corresponding power spectra in the low-frequency region; X axes are frequency in hertz and Y axes are spectral power in arbitrary units.

ily distinguished from the chamber not only in OPD figures but also in the figure of the power spectral density of OPD variations.

To study the time-dependence of the observed frequencies we applied the wavelet transform technique. Wavelet analysis of data series (e.g., time realizations of the OPD at a certain point of the cell) produces a so-called scalogram, a matrix of wavelet coefficients. With the wavelet coefficients one can calculate instantaneous and averaged power spectra. Figure 5(c) shows the scalogram for the OPD dynamics at the sixth point of the scan line crossing the neuron [a scheme of the neuron with the scan-line is shown in the bottom figures of Figs. 5(a) and 5(b)]. The original data (variations of OPD with time) are shown below the scalogram. In the scalogram one can see several pronounced rhythms in the region of 0 to 3 Hz. Frequencies of slow rhythms (around 0.1 and 0.2 to 0.5 Hz) remain relatively stable during the whole observation period, whereas rhythms of 0.8 to 1 and 2 to 3 Hz (marked by white curves) change their power and frequency. Variation of frequency of a biological process usually results from its modulation by other processes. To investigate such a nonlinear interaction we trace the dynamics of frequency and power of the rhythm and apply a second wavelet analysis. Rhythm tracing is done in the iWand. A rhythm is determined as a continuous succession of local maxima in the instantaneous power spectra. The time-dependence of the power and frequency rhythm is considered as an input signal for the second

wavelet analysis. As a result, we obtain the frequency and amplitude modulation spectra.¹¹

Figures 6(a) and 6(b) present time-averaged power spectra of the OPD changes in the boundary region of the leech neuron (sixth point of the scan line). Apparently, on the edges of the cell the column of integration [Eq. (4)] incorporates less cytoplasm height than in the cell center. Therefore, the membrane/cytoplasm ration is higher in the boundary region than in the cell center, and consequently the contribution of the membrane and submembrane processes to the RI dynamics is also higher in the cell boundary. Hence, in this case, we explore mainly membrane and submembrane processes. On the averaged spectra, we can also observe certain rhythms in the low-frequency range around 0.1, 0.2 to 0.5, 0.8 to 1, and 2 to 3 Hz [Fig. 6(b)], whereas there are no distinct pronounced rhythms in the high-frequency range. It does not seem likely, that the higher activity on the boundary should be ascribed to the lateral movements of the cell, as the cells under consideration lack active edge movements and adhere to the mirror surface; no substantial cell movements were observed during the entire of the experiment.

According to the literature, electrophysiological studies on isolated mollusk neurons show that these cells display intrinsic electrical activity: (1) changes of the membrane potential with 0.2 to 0.4-Hz frequencies caused by ion channel activity²³ and (2) intrinsic 1 and 1.5 to 3-Hz subthreshold and spontaneous electric activity.²⁴ Our previous studies showed

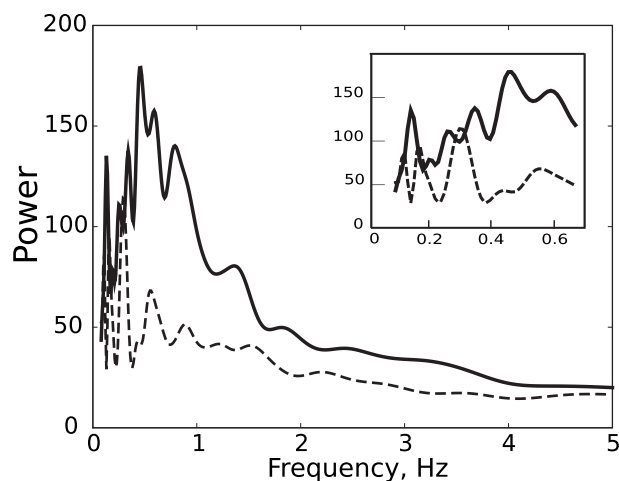


Fig. 7 Time-averaged power spectra of the plasma membrane-bound Ca^{2+} dynamics in R-neurons (solid line) and T-neurons (dashed line) of the medical leech. The inset figure shows enlarged part of the power spectrum in the low frequency region; X axis, frequency in hertz; Y axis, spectral power in arbitrary units.

that amplitude modulation of the rhythm around 1 Hz changes under membrane depolarization and hyperpolarization, indicating the dependence of the rhythm on the membrane potential¹²

To elucidate the origin of the observed rhythms we performed independent experiments in which we registered and did wavelet analysis of dynamics of the membrane-bound calcium ions. It is known that amount of Ca^{2+} ions bound on the surfaces of a plasma membrane depends on the ion channel activity and membrane potential.²⁵ Any modifications of the neuron electrical activity and transmembrane potential result in changes in the amount of plasma-membrane-bound Ca^{2+} ($\text{Ca}_{\text{mb}}^{2+}$). Therefore analysis of $\text{Ca}_{\text{mb}}^{2+}$ dynamics can provide additional information about membrane potential and ion channel activity. Fluorescent dye chlortetracycline (CTC) was used to register the $\text{Ca}_{\text{mb}}^{2+}$ amount. The intensity of CTC fluorescence depends on the level of plasma membrane-bound Ca^{2+} . Details of the technique can be found in Refs. 26 and 27. We studied dynamics of $\text{Ca}_{\text{mb}}^{2+}$ in two types of neurons of medical leech: Retzius neurons (R-neurons) and touch neurons (T-neurons). The characteristic feature of T-neurons is an extremely small number of voltage-dependent Ca^{2+} channels in the comparison with other neurons.²⁸ R-neurons possess very pronounced spontaneous activity and have a “normal” amount of Ca^{2+} channels.²⁹ Intensity of CTC fluorescence was recorded for 30 s with the sampling rate 62.5 Hz (the same as in PM-LIM experiments), and then we performed wavelet analysis of the obtained data. Figure 7 shows time-averaged power spectra of $\text{Ca}_{\text{mb}}^{2+}$ dynamics in R- and T-neurons. Each spectrum is an average of three independent experiments. In the case of R-neurons, there are intensive pronounced rhythms with maxima around 0.1, 0.4 to 0.6, and 0.8 to 1 Hz, whereas in T-neurons frequencies around 0.2 to 0.6 Hz have smaller power, and frequencies around 0.8 to 1 Hz tend to be absent. We suppose, that frequencies around 0.4 and 0.8 to 1 Hz observed in R-neurons result from ion channel activity (including Ca^{2+} channels) (0.4 Hz) and spontaneous electric

activity (0.8 to 1 Hz). This suggests that the origin of 0.2 to 0.6- and 0.8 to 1-Hz frequencies in the $\text{Ca}_{\text{mb}}^{2+}$ dynamics in neurons is the same as for the similar rhythms (0.2 to 0.5 and 1 Hz) in OPD dynamics.

Figures 6(c) and 6(d) present the characteristic dynamics of the OPD in a boundary of erythrocyte (discocyte). Note that low-frequency variations of the OPD are less pronounced compared to the neuron [Fig. 6(b)]. On the whole, the power spectra of the RI changes of the erythrocyte are weakly structured in both low- and high-frequency regions [Figs. 6(c) and 6(d)] with a relatively subtle rhythm below 0.1 to 0.2 Hz. We ascribe the weakness of rhythms to the rigid submembrane and membrane structures,³⁰ which prevent large-scale changes in the membrane and cytoplasm and, therefore, eliminate visible changes of the RI. Popescu et al. also studied changes of the erythrocyte OPD (re-calculated to the cell thickness) using means of Fourier phase microscopy, but at a lower frequency range, and demonstrated the existence of slow 0.1- to 0.5-min⁻¹ oscillations. We suppose that modification of the plasma membrane fluidity and the decrease in the rigidity of submembrane cytoskeleton can produce more pronounced frequencies in the ranges of >0.1 Hz.

6 Conclusion

We presented the application of phase-modulation laser interference microscopy to the noninvasive, nonstained live cell visualization and to the study of the RI dynamics in various cellular regions. Due to the independent measurement of the OPD at each pixel and to the phase image reconstruction algorithm that are implemented in the MIM 2.1 microscope it is possible to study OPD dynamics and to obtain phase images of different cell types from the simple cells such as erythrocytes to complicated cells with highly inhomogeneous cytoplasm such as neurons. We demonstrated that PM-LIM phase images of human erythrocytes show a clear difference between the discocytic and echinocytic form and that phase images of nucleated frog erythrocytes provide information about RI and, therefore, about Hb redistribution inside the cell during hemolysis.

Our results demonstrate that both neurons and erythrocytes exhibit regular changes in the OPD in the plasma membrane region. We suppose that in the case of neurons, these changes result mainly from the membrane processes: subthreshold dynamics of the membrane potential, ion channel activity, and possibly spontaneous firing. Results of independent experiments performed using fluorescent microscopy are in the accordance with suggestions about the origin of the rhythms observed in OPD dynamics. Interference cell imaging combined with wavelet analysis represents an advanced approach to understand the relations between multiple processes under normal and pathological conditions.

Acknowledgments

This work was partly supported by the European Commission (NoE BioSim, Contract No. 4SHB-CT-2004-005137). We are thankful to the Amphora Laboratories company (<http://www.amphoralabs.ru>) for providing the laser interference microscope MIM-2.1. N.B and A.B. acknowledge support from the Lundbeck Foundation and O.S. acknowledges a Skou grant from Forskningsraadet for Natur og Univers.

References

1. L. B. Cohen, R. D. Keynes, and B. Hille, "Light scattering and birefringence changes during nerve activity," *Nature (London)* **218**, 438–441 (1968).
2. R. A. Stepanoski, A. LaPorta, F. Raccaia-Behling, J. E. Blonder, R. E. Slusher, and D. Kleinfeld, "Noninvasive detection of changes in membrane potential in cultured neurons by light scattering," *Proc. Natl. Acad. Sci. U.S.A.* **88**, 9382–9386 (1991).
3. M. Haller, S. L. Mironov, and D. W. Richter, "Intrinsic optic signals in respiratory brain stem regions of mice: neurotransmitters, neuro-modulators, and metabolic stress," *J. Neurophysiol.* **86**, 412–421 (2001).
4. M. Lazebnik, D. L. Marks, K. L. Potgieter, R. Gillete, and S. A. Boppart, "Functional optical coherence tomography for detecting neural activity through scattering changes," *Opt. Lett.* **28**, 1218–1220 (2003).
5. V. A. Andreev and K. V. Indukaev, "The problem of subrayleigh resolution in interference microscopy," *J. Russ. Laser Res.* **24**, 220–236 (2003).
6. B. Rappaz, P. Marquet, E. Cuche, Y. Emery, C. Depeursinge, and P. J. Magistretti, "Measurement of the integral refractive index and dynamic cell morphometry of living cells with digital holographic microscopy," *Opt. Express* **13**, 9361–9373 (2005).
7. V. P. Tychinskii, "Coherent phase microscopy of intracellular processes," *Phys. Uspek.* **44**, 683–696 (2001).
8. G. Popescu, T. Ikeda, C. A. Best, K. Badizadegan, R. R. Dasari, and M. S. Feld, "Erythrocyte structure and dynamics quantified by Hilbert phase microscopy," *J. Biomed. Opt.* **10**, 060503 (2005).
9. G. Popescu, K. Badizadegan, R. R. Dasari, and M. S. Feld, "Observation of dynamic subdomains in red blood cells," *J. Biomed. Opt. Lett.* **11**, 040503 (2006).
10. G. Popescu, T. Ikeda, R. R. Dasari, and M. S. Feld, "Diffraction phase microscopy for quantifying cell structure and dynamics," *Opt. Lett.* **31**, 775–777 (2006).
11. O. V. Sosnovtseva, A. N. Pavlov, N. A. Brazhe, A. R. Brazhe, L. A. Erokhova, G. V. Maksimov, and E. Mosekilde, "Interference microscopy under double-wavelet analysis: a new approach to studying cell dynamics," *Phys. Rev. Lett.* **94**, 218103 (2005).
12. N. A. Brazhe, A. R. Brazhe, A. N. Pavlov, L. A. Erokhova, A. I. Yusipovich, G. V. Maksimov, E. Mosekilde, and O. V. Sosnovtseva, "Unravelling cell processes: interference imaging interwoven with data-analysis," *J. Biol. Phys.* **32**, 191–208 (2006).
13. V. A. Andreev and K. V. Indukaev, "Phase modulation microscope mim-2.1 for measurements of surface microrelief. general principles of design and operation," *J. Russ. Laser Res.* **26**, 380–393 (2005).
14. V. P. Tychinsky, "On superresolution of phase objects," *Opt. Commun.* **74**, 41–45 (1989).
15. V. Tychinsky, "Wavefront dislocations and registering images inside the Airy disk," *Opt. Commun.* **81**, 131–137 (1991).
16. M. Totzeck and H. J. Tiziani, "Interference microscopy of sub- λ structures: a rigorous computation method and measurements," *Opt. Commun.* **136**, 61–74 (1997).
17. M. Totzeck and H. J. Tiziani, "Phase-singularities in 2D diffraction fields and interference microscopy," *Opt. Commun.* **138**, 365–382 (1997).
18. V. A. Andreev, K. V. Indukaev, O. K. Ioselev, A. I. Legkii, G. L. Lasarev, and D. A. Orlov, "Phase modulation microscope mim-2.1 for measurements of surface microrelief. Results of measurements," *J. Russ. Laser Res.* **26**, 394–401 (2005).
19. H. G. Davies, "Structure in nucleated erythrocytes," *J. Biophys. Biochem. Cytol.* **9**, 671–687 (1961).
20. L. A. Erokhova, S. M. Novikov, G. L. Lazarev, T. A. Kazakova, D. A. Orlov, K. V. Indukaev, and G. V. Maksimov, "Study of regular intracellular and membrane processes in neurons by laser interference microscopy," *Bull. Exp. Biol. Med.* **140**, 262–264 (2005).
21. A. I. Yusipovich, S. M. Novikov, T. A. Kazakova, L. A. Erokhova, N. A. Brazhe, G. L. Lazarev, and G. V. Maksimov, "Peculiarities of studying an isolated neuron by the method of laser interference microscopy," *Quantum Electron.* **36**, 874–878 (2006).
22. A. Grossmann and J. Morlet, "Decomposition of hardy functions into square integrable wavelets of constant shape," *SIAM J. Math. Anal.* **15**, 723–736 (1984).
23. A. Szucs, G. Molnar, and K. S. Rozsa, "Periodic and oscillatory firing patterns in identified nerve cells of *Lymnaea stagnalis* L.," *Acta Biol. Hung.* **50**, 269–278 (1999).
24. A. Schutt, T. H. Bullock, and E. Basar, "Odor input generates 1.5 Hz and 3 Hz spectral peaks in the *Helix* pedal ganglion," *Brain Res.* **879**, 73–87 (2000).
25. B. Hille, "Ionic Channels of Excitable Membranes," University of Washington (1992).
26. N. A. Brazhe, L. A. Erokhova, A. A. Churin, and G. V. Maksimov, "The relation of different-scale membrane processes under nitric oxide influence," *J. Biol. Phys.* **31**, 531–546 (2005).
27. A. H. Caswell and J. D. Hutchinson, "Visualization of membrane-bound cations by a fluorescent technique," *Biochem. Biophys. Res. Commun.* **42**, 43–49 (1971).
28. K. Boev and N. Valkanov, "Differences in the kinetics of ionic currents in the somatic membrane of identified T- and N-mechanosensory neurons of medical leech," *Acta Physiol. Pharmacol. Bulg.* **14**, 67–76 (1988).
29. J. D. Angstadt, "Persistent inward currents in cultured retzius cells of the medicinal leech," *J. Comp. Physiol.* **184**, 49–61 (1999).
30. S. E. Lux and J. Palek, "Disorders of the red cell membrane," in *Blood Principles and Hematology*, R. I. Handin, S. E. Lux, and T. P. Stossel, Eds., pp. 1701–1818, JB Lippincott, Philadelphia, PA (1995).